Proton therapy treatment monitoring with in-beam PET: Investigating space and time activity distributions

L. Brombal[a,b,*], D. Barbosa[c,d], N. Belcari[c,d], M.G. Bisogni[c,d], N. Camarlinghi[c,d], L. Cristoforetti[e], A. Del Guerra[c,d], F. Fracchiolla[e], M. Morrocchi[c,d], G. Sportelli[c,d], R. Righetto[e], M. Schwarz[e,f], A. Topi[g,d], V. Rosso[c,d]

[a] *Department of Physics, University of Trieste, Trieste, Italy*
[b] *INFN- sezione di Trieste*
[c] *Department of Physics, University of Pisa, Pisa, Italy*
[d] *INFN- sezione di Pisa*
[e] *Proton Therapy Department, Trento Hospital, Trento, Italy*
[f] *TIFPA INFN, Trento, Italy*
[g] *Department of Physical Sciences, Earth and Environment, University of Siena, Siena, Italy*

ARTICLE INFO

Keywords:
Particle Therapy
In-beam monitoring
PET

ABSTRACT

In this study the possibility of retrieving composition information in proton therapy with a planar in-beam PET scanner is investigated. The analysis focuses both on spatial activity distributions and time dependence of the recorded signal. The experimental data taking was performed at the Trento Proton Therapy Center (IT) by irradiating three different phantoms. We show that different phantom compositions reflect into different activity profile shapes. We demonstrate that the analysis of the event rate can provide significant information on the phantom elemental composition, suggesting that elemental analysis could be used along with activity profile analysis to achieve a more accurate treatment monitoring.

1. Introduction

Radiotherapy is one of the key players in modern cancer treatment and roughly 45–55% of cancer patients require radiotherapy at some point [1]. The goal of the treatment is to deliver a high conformal dose to the tumor region, minimizing the dose to the surrounding tissues.

Proton therapy is a leading edge radiotherapy technique which allows the delivery of high-dose in well-defined volumes (Bragg-peak) significantly reducing the absorbed dose in the sorroundings. However, due to the steep dose profile of protons, this technique is much more sensitive to spatial uncertainties than conventional photon treatments. In fact, uncertainties in particle range, unexpected anatomical changes and patient or accelerator setup errors, may cause either severe over- or under-dosage in the target or increased dose in adjacent tissues [2,3]. For this reason, a system which allows to monitor the treatment would be highly desirable. Since protons stop in the patient, in-vivo treatment monitoring requires detecting secondary radiation.

So far, Positron Emission Tomography (PET) is the most studied monitoring technique [4–9]. It is based on the detection of back-to-back photons (511 keV) originating from e- e+ annihilation: in protontherapy the positron arises from β+ emitters (mainly ^{11}C and ^{15}O) generated by nuclear interaction between protons and the patient tissues. Actually, nuclear interactions at clinically used energies produce also other secondary particle as prompt gamma rays and charged particle which can be used for monitoring purposes: recently the first clinical application of a prompt gamma based monitoring system has been performed [10], while systems using charged particles are under investigation [11–13]. A detailed review about nuclear interactions in particle therapy can be found in [14]. For PET the recorded signal, i.e., the isotopic activity, is only indirectly related to the delivered dose, although a useful information on the proton range can be inferred [15–17]. Furthermore, since the recorded signal and the tissue composition are directly related, the analysis of activity profiles and signal time dependence can provide extra-information on the elemental composition of the irradiated object. The latter kind of analysis, in which the detected coincidence rate as a function of time is studied, will hereinafter referred to as elemental analysis.

In this study a large area dual head PET prototype developed and built in Pisa is used. The system is an upgraded version of DoPET prototype [18] with an active area of about 15×15 cm^2 which allows to

* Correspondence to: University of Trieste, Building F, Via Valerio, 2, 34127 Trieste, Italy.
E-mail address: luca.brombal@ts.infn.it (L. Brombal).

http://dx.doi.org/10.1016/j.nima.2017.05.002
Received 8 March 2017; Received in revised form 27 April 2017; Accepted 2 May 2017
Available online 03 May 2017

cope with volumes encountered in the clinical practice. Irradiations were performed at the cyclotron of Trento Proton Therapy Center using plastic phantoms.

The aim of this work is to investigate the DoPET capability of providing information on the irradiated phantom compositions both in space and in time domains.

2. Materials and methods

2.1. PET system

The present system is based on an upgraded version of DoPET prototype where new ten modules were built and added to the previous eight modules detector. Each head covers an area of about 15×15 cm^2 and it is composed by 9 independent modules. Each module consists of a 23×23 LYSO crystal matrix (~2 mm pitch) each one coupled to a 8×8 multianode position sensitive photomultiplier Hamamatsu H8500. The signal readout is performed by a custom front-end electronics connected to a FPGA, which embeds a coincidence processor with a time window of 3 ns [19]. The distance between the two heads was set to 48 cm. A more detailed description of the system can be found in [20,21].

2.2. Phantom irradiation

In this study 3 different phantoms were irradiated. Two of them are a homogeneous slab of PMMA and of brain equivalent tissue (hereinafter referred to as BRAIN) with a transverse section of 5×5 cm^2 and a length of 14 cm along the beam direction. The other test object, named ZEBRA, is made up of 4 slices of PMMA and 2 of BRAIN alternated along the beam axis (see Fig. 1). All the phantoms are inserted in a PMMA holder bringing to a final phantom dimension of $8 \times 8 \times 14$ cm^3. Density and chemical composition of PMMA and BRAIN are reported in Table 1. All the phantoms were irradiated with a 130 MeV pencil beam with a gaussian transversal profile (FWHM≃10 mm). Irradiations where performed with high (10^{10} protons) and low (10^9 protons) statistics, corresponding respectively to an entrance dose of 800 cGy and 80 cGy and delivery times of 14 s and 2 s.

2.3. Data processing

PET data are acquired in form of photon pairs detected in a coincidence time window of 3 ns within the energy window [350, 850] keV. Each pair defines a line-of-response (LOR), and it is stored in a file containing the number of hit detected for each LOR. To obtain the 3-D activity image these data first undergo to a normalization procedure, based on an flat-field acquisition of a homogeneous

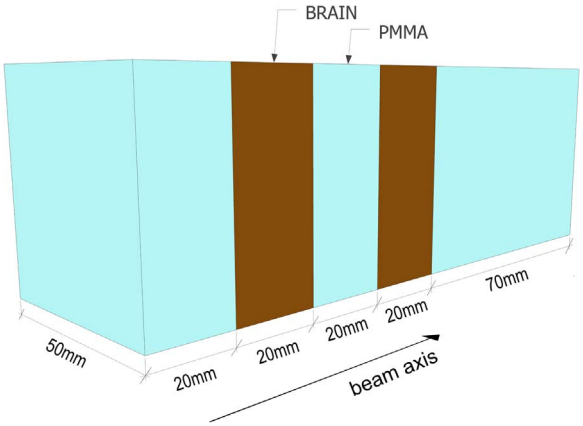

Fig. 1. 3D view of ZEBRA phantom: light blue slabs are PMMA, brown slabs are BRAIN. (For interpretation of the references to color in this figure legend, the reader is referred to the web version of this article.)

Table 1
Density and chemical composition (fraction by weight) of the used materials.

Material	ρ (gcm^{-3})	H (%)	C (%)	O (%)	N (%)
PMMA	1.18	8.06	59.98	31.96	–
BRAIN	1.05	10.83	72.54	14.56	1.69

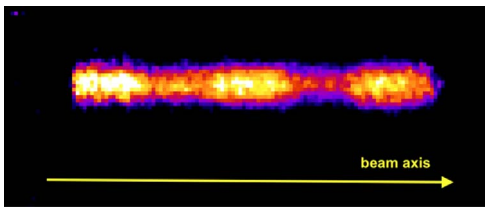

Fig. 2. ZEBRA phantom irradiation: image of the activated volume in the sagittal plane.

planar phantom filled with ^{18}FDG [22], and subsequently are processed using a Maximum-Likelihood-Expectation-Maximization algorithm [23] which makes use of an analytical model of the system matrix. The reconstructed field of view (FOV) has a volume of 10×16×16 cm^3, segmented into 1 mm^3 voxels. Images can be extracted in different planes: an example of a sagittal plane view is shown in Fig. 2.

When only elemental analysis is required, the reconstruction process is not needed and the raw data, expressed as coincidence rate as a function of time, acquired over the whole FOV can be used. In this case a random coincidences subtraction process, based on the delayed window technique, is applied [24]. For each irradiation data were acquired for 550 s after the beam is turned off (beam-off period).

2.4. Data analysis

For all the experiments presented in our study data analysis has a dual purpose: the profile analysis is aimed to extract information about the location of the activated material within the phantom while the elemental analysis highlights composition differences among the phantoms.

2.4.1. Profile analysis

Images are reconstructed using data collected within 120 s after the end of the irradiation: 1-D activity profiles are obtained projecting all the events included in an elliptical ROI in the transverse plane on the z axis, that represents the beam axis (see also [18]). This procedure is suggested by the geometrical configuration of DoPET which, as discussed in Section 2.1, is based on two planar heads. Such configuration makes the beam axis a privileged direction, i.e., the direction with the maximal spatial resolution corresponding to 1.5 mm [25]. This kind of analysis allows us to recover spatial information on the activation and, from the temporal point of view, it provides an integrated information.

2.4.2. Elemental analysis

Elemental analysis is carried out using the data collected during the whole acquisition time of 550 s. Since the recorded activity is due to β+ radioactive decays, the decrease in the coincidence rate after the irradiation is a sum of exponential decays, a different one for each produced isotope. Hence the beam-off signal is fitted with:

$$f(t) = \sum_i a_i \exp\left(-\frac{t \ln(2)}{T_i}\right), \quad (1)$$

where t is the time elapsed from the end of the irradiation, a_i is a free parameter and T_i is the half-life of each isotope.

Once the fit has been performed the percent contribution of a given isotope to the overall signal (C_i) in a given time window [t_1, t_2] is computed as:

Table 2
Relevant reaction channels [7,26]. Energies labelled with * are calculated in the laboratory reference frame using relativistic conservation of energy-momentum and imposing the threshold condition, i.e., the products have null kinetic energy in the center of mass reference frame.

Isotope	Half-life (s)	Channel	Threshold (MeV)
^{11}C	1220	$^{12}C(p,pn)^{11}C$	20.61
		$^{16}O(p,\ 3p3n)^{11}C$	59.64
^{10}C	19.3	$^{12}C(p,p2n)^{10}C$	35*
		$^{16}O(p,3p4n)^{10}C$	72*
^{15}O	122.2	$^{16}O(p,pn)^{15}O$	16.79
^{8}B	0.770	$^{12}C(p,2p3n)^{8}B$	61*

$$C_i(\%) = \frac{\int_{t_1}^{t_2} a_i \exp\left(-\frac{t\ln(2)}{T_i}\right)\mathrm{d}t}{\int_{t_1}^{t_2} f(t)\mathrm{d}t} \times 100, \tag{2}$$

where t_1 refers to the beginning of the beam-off period and $t_2 = t_1 + 550$ s. The error associated to each contribution derives from the uncertainty of the estimated parameters a_i, propagated using the standard error propagation rules.

According to the chemical composition of our phantoms, the most relevant expected β+ emitters, along with their reaction channels, are summarized in Table 2.

This kind of analysis allows us to recover time information at the expenses of spatial information: in fact, the whole FOV is considered, i.e., the signal is spatially integrated.

3. Results and discussion

3.1. Activity profiles

In Fig. 3 the activity profiles along z-axis of the three phantoms obtained with high statistics (i.e., 10^{10} protons) are reported. All the shown profiles represent the reconstructed statistics and the amplitudes are strictly related to the number of impinging protons. It is clear that while the profiles of homogeneous phantoms (square markers for PMMA and triangle markers for BRAIN) are quite uniform, the profile of the ZEBRA phantom (filled area) presents two activity deficits each about 20 mm wide. The location of these details, respectively at 20 and 60 mm from the phantom entrance, coincides with the actual location of the BRAIN slabs. From the profile reported in Fig. 4 the width of the BRAIN slabs are estimated by fitting the edges of the activity defects

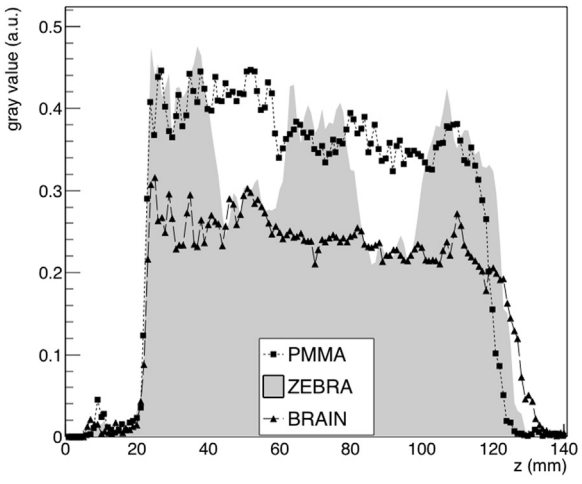

Fig. 3. Activity profiles of PMMA, ZEBRA and BRAIN phantoms irradiated with 10^{10} protons: the z coordinate corresponds to the beam axis. Square points refers to PMMA, triangles to BRAIN and grey area to ZEBRA phantom. Profiles are obtained integrating the signal in the (0, 120 s) time window.

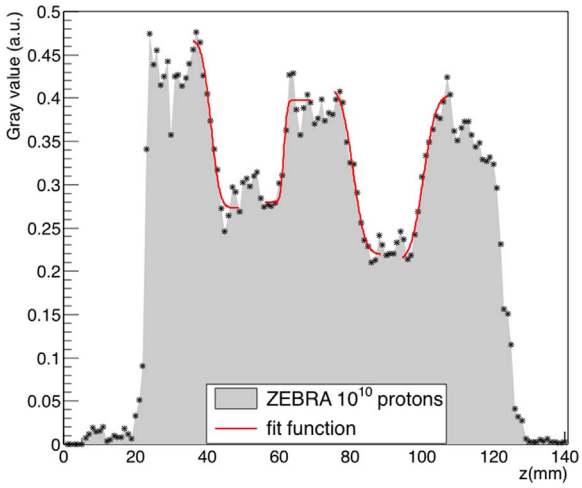

Fig. 4. Activity profiles of ZEBRA phantom obtained with 10^{10} protons: the edges of the activity deficits corresponding to the presence of BRAIN slabs are fitted with error functions (red). (For interpretation of the references to color in this figure legend, the reader is referred to the web version of this article.)

with an error function. If we compute the difference between the 50% of the profile rise and fall, the resulting widths are 20.4 ± 0.5 mm for the first slab and 19.7 ± 0.6 mm for the second one. These values are well compatible with the actual width (20 mm) of the BRAIN slabs. Furthermore, the amplitude of the ZEBRA profile corresponds to that of homogeneous PMMA profile where PMMA slabs are located and to the homogeneous BRAIN profile where BRAIN slabs are present. So, comparing the ZEBRA profile with the homogeneous ones, we have both a spatial and composition information along the beam axis. Moreover, as it should be expected, the activity fall-off edges of the three phantoms depend on the phantom density: the less dense phantom (BRAIN) has a deeper activity fall-off.

The lower activity signal of BRAIN with respect to PMMA is mainly due to the lower percentage of oxygen (see Table 1) together with the chosen time window. In fact, if we reconstruct the activity distribution of the ZEBRA phantom integrating the signal at later times, from 300 to 550 s after the end of the irradiation, we obtain the profile reported in Fig. 5: in this case the oxygen signal is almost lost and the BRAIN slabs cannot be distinguished from the PMMA.

The previous results are encouraging but they are obtained using a high statistic pencil beam. To move to pencil beams that are more commonly encountered in clinical practice when hypofractionation

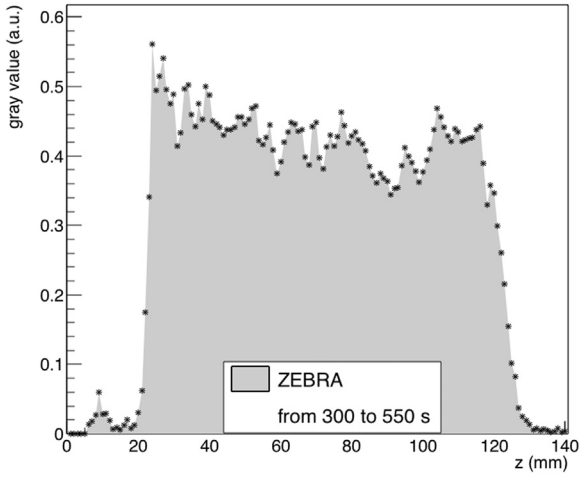

Fig. 5. Activity profiles of ZEBRA phantoms obtained with 10^{10} protons: the edges of the activity deficits corresponding to the presence of BRAIN slabs are fitted with error functions. Profile is obtained integrating the signal in the [300,550] s time window.

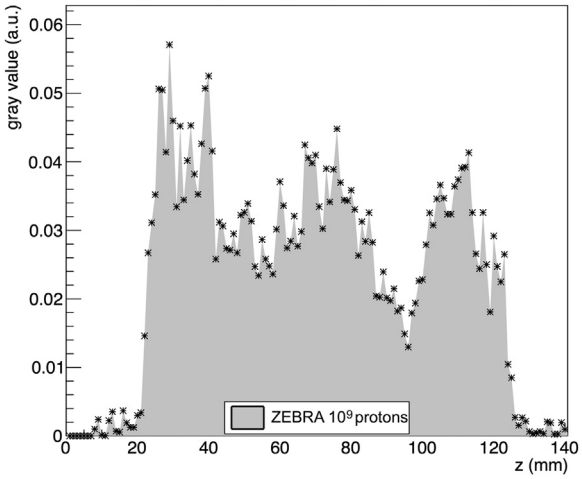

Fig. 6. Activity profiles of ZEBRA phantom obtained with 10^9 protons in the 0,120] s time window: it is not possible to clearly identify the presence of BRAIN slabs.

schemes are applied, the ZEBRA phantom was irradiated also with a beam containing 10^9 protons: the resulting profile is reported in Fig. 6. As we should expect the profile intensity is one order of magnitude lower than the high statistics irradiation. In this case the profile is dominated by noise and, even if the presence of two activity defects can be observed, neither the exact location nor the dimension of this cavities can be unambiguously deduced.

3.2. Temporal profiles

In Fig. 7(a)–(c), the coincidence rate as a function of time recorded during the beam-off period of the high statistics irradiation are shown. These data are fitted with the function reported in Eq. (2) including all the 4 isotopes listed in Table 2. As it is clear from the figures, the best fit function includes the contributions of ^{11}C, ^{15}O, ^{10}C, ^{8}B where, as expected, the fist two isotopes are the most abundant ones. The presence of these 4 isotopes is also reported in other experiments where 55 MeV protons impinging on a PMMA phantom and an ad-hoc experimental setup for time analysis are used [27]. From Fig. 8, which displays only the first 270 s after the irradiation, it can be inferred that moving from PMMA (top) to BRAIN phantom (bottom) the contribution of ^{15}O reduces by a factor 2 while ^{11}C slightly increases: this behavior reflects the different composition of the two phantoms. Quantitative considerations can be drawn observing Fig. 9, where only the percent contribution of ^{11}C and ^{15}O are considered since they constitute more than 90% of the recorded signal. In the graph we can see that the contribution of ^{15}O and ^{11}C of the ZEBRA phantom are intermediate between the PMMA and BRAIN phantoms. Furthermore, for each phantom pair, the percent differences are statistically significant, i.e., they exceed 3 standard deviations. The same analysis is repeated for the low statistics irradiation of the ZEBRA phantom (also

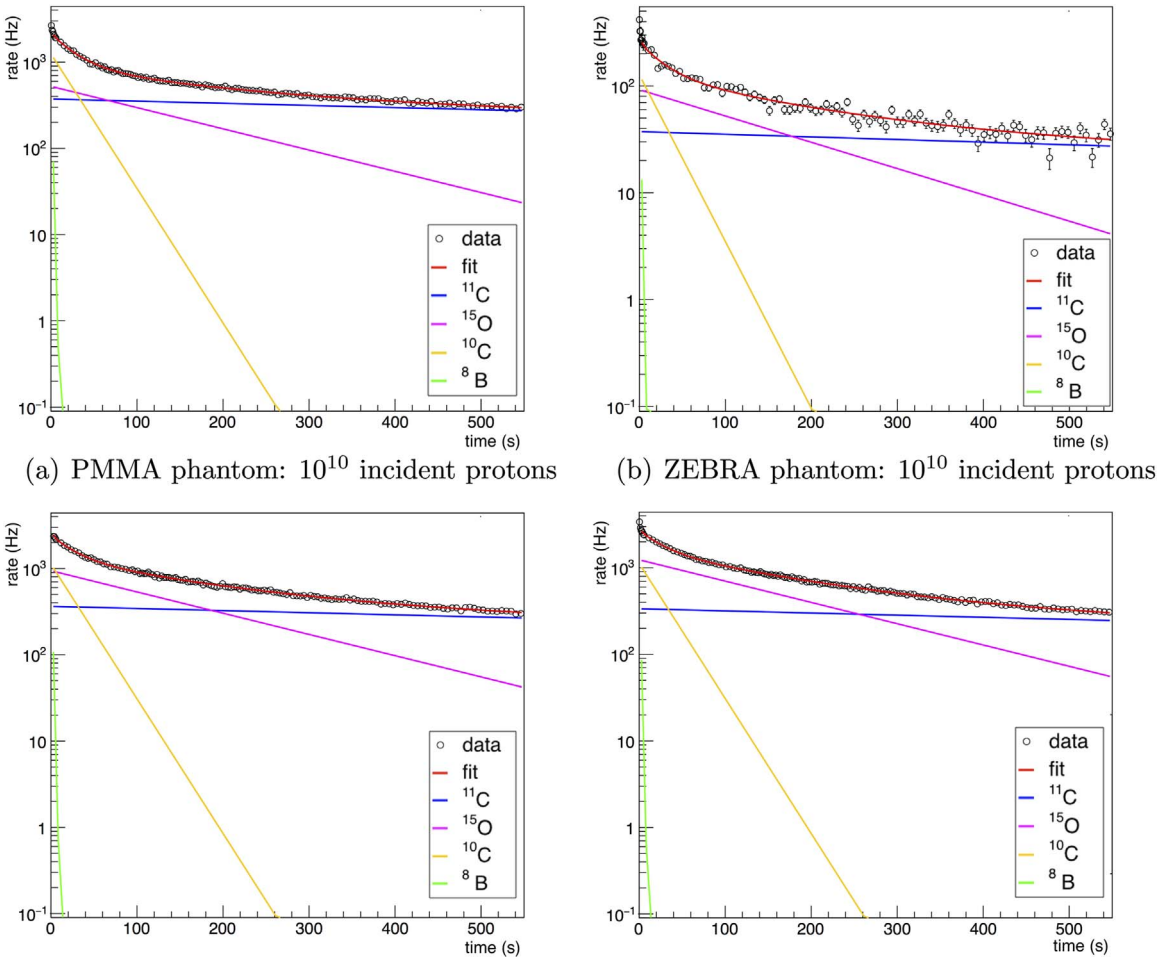

(a) PMMA phantom: 10^{10} incident protons

(b) ZEBRA phantom: 10^{10} incident protons

(c) BRAIN phantom: 10^{10} incident protons

(d) ZEBA phantom: 10^9 incident protons

Fig. 7. Recorded coincidence rate as a function of time for all the irradiations. Red line represents the fit function, other lines correspond to each isotopic contribution. Error bars are visible only in (d) for long times, in the other cases they are smaller than points. (For interpretation of the references to color in this figure legend, the reader is referred to the web version of this article.)

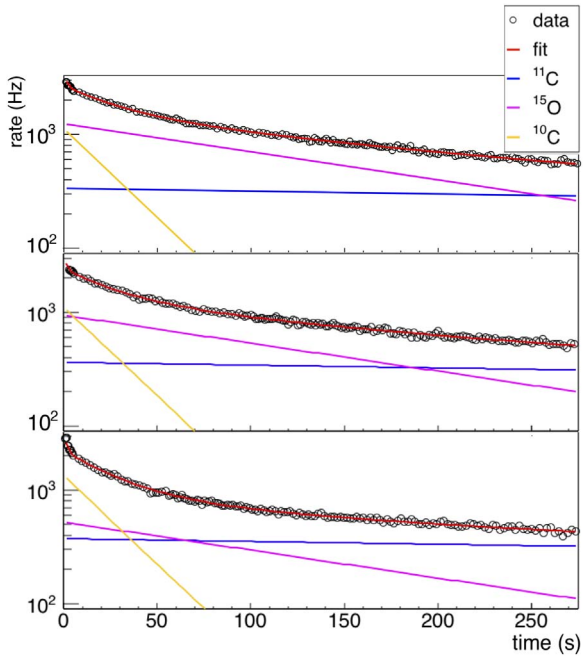

Fig. 8. Zoom view for the coincidence rate in [0,270] s time window. Top: PMMA homogeneous phantom. Central: ZEBRA phantom. Bottom: BRAIN homogeous phantom.

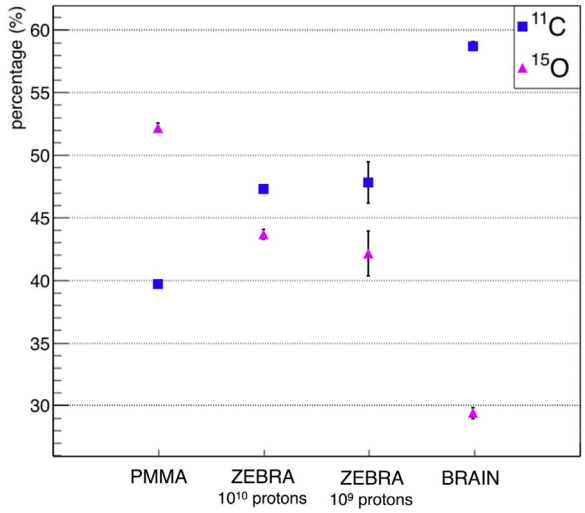

Fig. 9. Percentages of ^{15}O and ^{11}C for all the studied irradiations.

reported in Fig. 7(d)). In this case, even if the statistics is reduced by a factor 10, the percent contributions are still compatible with the high statistics irradiations and significantly different from those of BRAIN and PMMA phantoms. Thus, within the reported experimental conditions, elemental analysis can provide useful information of the phantom composition also with a lower proton statistics with respect to profile analysis. For the sake of completeness, Table 3 reports the isotope percentages found in each irradiation.

4. Conclusions

This study investigated the capability of a PET monitoring prototype, i.e., DoPET, in discriminating different irradiated material both in space and time domains, with the aim to bring useful indications for the monitoring practice in proton therapy.

The comparison between the profile obtained integrating the signal in a time window starting right after the irradiation [0,120] s and that at later times [300,550] s, shows that the capability to acquire the ^{15}O signal is relevant not only for statistical reasons but is also crucial to correctly discriminate the materials. So monitoring systems located strictly close to the irradiated patient, i.e, in-beam systems, are advantageous. The 1-D activity profiles analysis revealed that, irradiating with a high dose pencil beam a PMMA phantom where 2 slabs of brain equivalent tissue are inserted, the system is capable of detecting the presence of materials that differ in oxygen composition, moving from about 15–32%, allowing a correct estimate of the slab widths. The imaging capabilities are reduced when the dose is lowered by a factor 10 since the profile noise becomes predominant not allowing a clear detection of the inserted slabs. This is a clear indication that more than a direct imaging of the activated volume, as the PET signal is generated from low statistics processes, a comparison between expected and measured activity is advised. So the use of a Monte Carlo simulation codes able to calculate the expected activity distribution is mandatory.

Along with 1-D activity distribution analysis, another approach to retrieve elemental composition information was investigated. In fact, studying the recorded coincidence rate as a function of time the production of 4 β+ emitters (i.e., ^{11}C, ^{15}O, ^{10}C, ^{8}B) was evidentiated. Considering only the most abundant isotopes, namely ^{11}C and ^{15}O, it was shown that their percentage varies accordingly to the phantom composition, i.e., they provide information on the phantom. The results obtained analyzing the low dose irradiation are consistent with the high dose data, hence the elemental analysis is found to be less dependent on the proton statistics with respect to the profile analysis. Here we remark that, in the context of treatment monitoring, also these data, which are obtained from a direct measurement of the irradiated object, can be compared with Monte Carlo predictions to access whether the treatment was correctly delivered or not.

On the other hand, the capability to detect specific isotopes can be useful. In particular, being able to detect short-lived isotopes (e.g., ^{37}K and ^{38}K) produced irradiating tissues containing calcium, it would be possible to state if the irradiation of a bone structure took place: this signature is relevant for cases in which the bone structure is adjacent to the target volume but has to be avoided from irradiation.

Future developments of the presented analysis require, first of all, the development of new electronics to cope with the need to detect short-lived isotopes. Then, a more in-depth study using anthropomorphic phantoms will be performed to investigate whether the comparison with Monte Carlo predictions together with isotopic analysis, allows to reduce the margins for range uncertainties currently used in the definition of the target volume. This technique could be first tested in clinical practice in the context of hypofractionation schemes, selecting specific pencil beams from the treatment plan.

Table 3
Percent isotopic contribution to the overall signal within 550 s from the irradiation end.

phantom type	^{11}C (%)	^{15}O (%)	^{10}C (%)	^{8}B (%)	TOT (%)
PMMA	39.75 ± 0.29	52.19 ± 0.37	7.80 ± 0.14	0.26 ± 0.02	100
BRAIN	58.71 ± 0.37	20.41 ± 0.42	11.57 ± 0.17	0.31 ± 0.03	100
ZEBRA 10^{10}	47.32 ± 0.32	43.70 ± 0.39	8.59 ± 0.16	0.39 ± 0.20	100
ZEBRA 10^9	47.82 ± 1.65	42.14 ± 1.79	9.56 ± 0.61	0.48 ± 0.07	100

References

[1] E. Rosenblatt, J. Izewska, Y. Anacak, Y. Pynda, P. Scalliet, M. Boniol, P. Autier, Radiotherapy capacity in european countries: an analysis of the directory of radiotherapy centres (dirac) database, Lancet Oncol. 14 (2) (2013) e79–e86.

[2] H. Paganetti, Range uncertainties in proton therapy and the role of Monte Carlo simulations, Phys. Med. Biol. 57 (11) (2012) R99.

[3] A.-C. Knopf, A. Lomax, In vivo proton range verification: a review, Phys. Med. Biol. 58 (15) (2013) R131.

[4] W. Enghardt, J. Debus, T. Haberer, B. Hasch, R. Hinz, O. Jäkel, M. Krämer, K. Lauckner, J. Pawelke, F. Pönisch, Positron emission tomography for quality assurance of cancer therapy with light ion beams, Nucl. Phys. A 654 (1) (1999) 1047c–1050c.

[5] T. Nishio, A. Miyatake, T. Ogino, K. Nakagawa, N. Saijo, H. Esumi, The development and clinical use of a beam ON-LINE PET system mounted on a rotating gantry port in proton therapy, Int. J. Radiat. Oncol.* Biol.* Phys. 76 (1) (2010) 277–286.

[6] K. Parodi, PET monitoring of hadrontherapy, Nucl. Med. Rev. 15 (2012) 7–13.

[7] X. Zhu, G.E. Fakhri, Proton therapy verification with PET imaging, Theranostics 3 (10) (2013) 731–740.

[8] G. Sportelli, N. Belcari, N. Camarlinghi, G. Cirrone, G. Cuttone, S. Ferretti, A. Kraan, J. Ortuño, F. Romano, A. Santos, et al., First full-beam PET acquisitions in proton therapy with a modular dual-head dedicated system, Phys. Med. Biol. 59 (1) (2013) 43.

[9] A. Del Guerra, N. Belcari, M. Bisogni, Positron emission tomography: its 65 years, Riv. Nuovo Cim. 39 (2016) 155.

[10] C. Richter, G. Pausch, S. Barczyk, M. Priegnitz, I. Keitz, J. Thiele, J. Smeets, F. Vander Stappen, L. Bombelli, C. Fiorini, et al., First clinical application of a prompt gamma based in vivo proton range verification system, Radiother. Oncol. 118 (2) (2016) 232–237.

[11] L. Piersanti, F. Bellini, F. Bini, F. Collamati, E. De Lucia, M. Durante, R. Faccini, F. Ferroni, S. Fiore, E. Iarocci, et al., Measurement of charged particle yields from PMMA irradiated by a 220 MeV/u 12 C beam, Phys. Med. Biol. 59 (7) (2014) 1857.

[12] M. Marafini, P. Frallicciardi, R. Faccini, C. Morone, C. Voena, V. Patera, L. Piersanti, A. Sciubba, A. Attili, S. Coli, et al., The INSIDE project: Innovative solutions for in-beam dosimetry in hadrontherapy., Acta Phys. Pol. A 127 (5).

[13] M.G. Bisogni, A. Attili, G. Battistoni, N. Belcari, P. Cerello, S. Coli, A. Del Guerra, A. Ferrari, V. Ferrero, E. Fiorina, et al., INSIDE in-beam positron emission tomography system for particle range monitoring in hadrontherapy, J. Med. Imaging 4 (1) (2017) 011005.

[14] M. Durante, H. Paganetti, Nuclear physics in particle therapy: a review, Rep. Progr. Phys. 79 (9) (2016) 096702.

[15] K. Parodi, W. Enghardt, Potential application of pet in quality assurance of proton therapy, Phys. Med. Biol. 45 (11) (2000) N151.

[16] H. Tashima, T. Yamaya, E. Yoshida, S. Kinouchi, M. Watanabe, E. Tanaka, A single-ring OpenPET enabling PET imaging during radiotherapy, Phys. Med. Biol. 57 (14) (2012) 4705.

[17] V. Rosso, G. Battistoni, N. Belcari, N. Camarlinghi, M. Ciocca, F. Collini, S. Ferretti, A. Kraan, S. Lucenò, S. Molinelli, et al., In-treatment tests for the monitoring of proton and carbon-ion therapy with a large area PET system at CNAO, Nucl. Inst. Methods Phys. Res. Sect. A: Accel. Spectrometers Detect. Assoc. Equip. 824 (2016) 228–232.

[18] A. Kraan, G. Battistoni, N. Belcari, N. Camarlinghi, G. Cirrone, G. Cuttone, S. Ferretti, A. Ferrari, G. Pirrone, F. Romano, et al., Proton range monitoring with in-beam PET: Monte Carlo activity predictions and comparison with cyclotron data, Phys. Med. 30 (5) (2014) 559–569.

[19] G. Sportelli, N. Belcari, P. Guerra, A. Santos, Low-resource synchronous coincidence processor for positron emission tomography, Nucl. Inst. Methods Phys. Res. Sect. A: Accel. Spectrometers Detect. Assoc. Equip. 648 (2011) S199–S201.

[20] S. Vecchio, F. Attanasi, N. Belcari, M. Camarda, G.P. Cirrone, G. Cuttone, F. Di Rosa, N. Lanconelli, S. Moehrs, V. Rosso, et al., A PET prototype for in-beam monitoring of proton therapy, IEEE Trans. Nucl. Sci. 56 (1) (2009) 51–56.

[21] G. Sportelli, N. Belcari, P. Guerra, F. Spinella, G. Franchi, F. Attanasi, S. Moehrs, V. Rosso, A. Santos, A. Del Guerra, Reprogrammable acquisition architecture for dedicated positron emission tomography, IEEE Trans. Nucl. Sci. 58 (3) (2011) 695–702.

[22] N. Camarlinghi, G. Sportelli, G. Battistoni, N. Belcari, M. Cecchetti, G. Cirrone, G. Cuttone, S. Ferretti, A. Kraan, A. Retico, et al., An in-beam PET system for monitoring ion-beam therapy: test on phantoms using clinical 62 MeV protons, J. Instrum. 9 (04) (2014) C04005.

[23] S. Moehrs, M. Defrise, N. Belcari, A. Del Guerra, A. Bartoli, S. Fabbri, G. Zanetti, Multi-ray-based system matrix generation for 3D PET reconstruction, Phys. Med. Biol. 53 (23) (2008) 6925.

[24] N. Belcari, F. Attanasi, S. Moehrs, V. Rosso, A. Santos, F. Spinella, G. Sportelli, A. Del Guerra, A novel random counts estimation method for PET using a symmetrical delayed window technique and random single event acquisition, in: Proc. IEEE NSS/MIC Conf, 2009, pp. 3611–3614.

[25] E. Fabbiani, N. Belcari, N. Camarlinghi, A. Del Guerra, S. Ferretti, A. Kraan, D. Panetta, G. Sportelli, V. Rosso, Performance evaluation of a LYSO-based PET scanner for monitoring of dose delivery in hadrontherapy, J. Instrum. 10 (12) (2015) C12029.

[26] S. Espana, X. Zhu, J. Daartz, G. El Fakhri, T. Bortfeld, H. Paganetti, The reliability of proton-nuclear interaction cross-section data to predict proton-induced PET images in proton therapy, Phys. Med. Biol. 56 (9) (2011) 2687.

[27] P. Dendooven, H. Buitenhuis, F. Diblen, P. Heeres, A. Biegun, F. Fiedler, M. van Goethem, E. van der Graaf, S. Brandenburg, Short-lived positron emitters in beam-on PET imaging during proton therapy, Phys. Med. Biol. 60 (23) (2015) 8923.